RESEARCH ARTICLE | MAY 22 2023

Vortex-Induced vibration suppression for a cylinder with random grooves inspired by rough tree bark

Zhang Baoshou (张宝收) ; Long Teng (龙腾) ; Wang Wei (王伟) ; Shi Renhe (史人赫); Ye Nianhui (叶年辉)

Physics of Fluids 35, 057125 (2023)
https://doi.org/10.1063/5.0152120

Physics of Fluids ARTICLE pubs.aip.org/aip/pof

Vortex-Induced vibration suppression for a cylinder with random grooves inspired by rough tree bark

Cite as: Phys. Fluids **35**, 057125 (2023); doi: 10.1063/5.0152120
Submitted: 28 March 2023 · Accepted: 5 May 2023 ·
Published Online: 22 May 2023

Baoshou Zhang (张宝收),[1] Teng Long (龙腾),[1,a)] Wei Wang (王伟),[2] Renhe Shi (史人赫),[1] and Nianhui Ye (叶年辉)[1]

AFFILIATIONS

[1]School of Aerospace Engineering, Beijing Institute of Technology, Beijing 100081, China
[2]Department of Mechanical Engineering, The Hong Kong Polytechnic University, Hung Hom, Kowloon, Hong Kong, China

[a)]Author to whom correspondence should be addressed: tenglong@bit.edu.cn

ABSTRACT

The vortex-induced vibration (VIV) response of a 2-degree-of-freedom cylinder with random grooves is investigated numerically based on the Reynolds Average Navier–Stokes (RANS) method. The Newmark-β method is used to solve the equations of motion of the cylinder. The effects of the random groove on VIV suppression are discussed in detail. The coverage ratios (k) of the random groove include 0%, 25%, 50%, 75%, and 100%. The vibration suppression effect of $k = 75\%$ and $k = 100\%$ is not significant. However, the VIV amplitude of the cylinders with $k = 25\%$ is greatly suppressed. In particular, the cross-flow amplitude ratio is reduced from 1.50 ($k = 0\%$, a smooth cylinder) to 0.65 ($k = 25\%$). First, the boundary-layer separation point of the grooves is fixed, so the random grooves destroy the normal separation and development of the main vortices. Therefore, two rows of vortices with different sizes are generated on both sides of the cylinder, which may cause unstable vibration. Meanwhile, a series of small vortices are formed in the grooves. These small vortices cannot merge synchronously into the main vortices and further reduced the strength of the main vortices. Consequently, the driving force of the vibration, which is generated by the main vortices, is reduced. As a result, the VIV responses are suppressed.

I. INTRODUCTION

In a constant flow, the vibration response of a non-streamline object will be induced by alternate shedding vortices, and the vibration will also affect the shape of the shedding vortex.[1] This interaction phenomenon between the structure and fluid is called vortex-induced vibration (VIV).[2] When the vortex shedding frequency is close to the natural frequency of the structure, "locking" or vortex synchronization occurs. This is an important cause of structural instability and fatigue failure.[3,4] There are many cases of structural damage caused by VIV in the ocean engineering, aerospace, and construction industries.[5,6] In the transportation of ocean oil and gas resources, cylindrical structures (marine risers, etc.) are widely used.[7] The cylindrical structures are prone to structural instability due to the VIV responses.[8,9] Similarly, VIV responses have been an important consideration for bridge designers.[10,11] Therefore, the research on the VIV suppression method for cylindrical structures has received a lot of attention from the engineering community.

In recent years, a lot of experimental and numerical studies have been conducted on VIV suppression. VIV suppression methods are commonly divided into active control and passive control. If there is external energy input, the VIV suppression method belongs to the active control method; if not, it is a passive control method. For active control, Wan and Patnaik studied the influence of the thermal effects on the suppression of the transverse vortex-induced vibration (VIV).[12] The amplitude of VIV obvious was suppressed with the increasing thermal control parameter Richardson number. Hasheminejad and Masoumi proposed a method of the hybrid active/semi-active cross-flow vortex-induced vibration (VIV) suppression.[13] They used the smart actively rotating control rods to reduce the displacement (68%), lift amplitudes (61%), and drag coefficients (12%). In addition, it is possible to control the flow around bluff bodies by generating a secondary flow. Fluid flow around a square obstacle with uniform suction and blowing was numerically controlled by Sohankar *et al.*[14] They found that when the suction is employed on the top and bottom surfaces and blowing is applied on the front and rear faces, optimum control can be achieved. Rabiee investigated the difference between the active open-loop and closed-loop control approaches on the control of

the VIV. Among them, the closed-loop control approach is more desirable.[15] In addition, control of vortex shedding by rotary oscillations is also an efficient way. In this method, the near-wake structure is importantly modified by the interaction between the surrounding fluid and the rotationally oscillating surface. Flinois and Colonius suppressed the vortex shedding of a cylinder utilizing body rotation.[16] Zhu *et al.* controlled the vortex-induced vibration of a circular cylinder using a pair of air jets and reported a more than 60% reduction in transverse amplitude is achieved.[17] Meanwhile, the control of vortex-induced vibration VIV of an elastically mounted cylinder with a pair of porous rods is numerically investigated by Chen and Wu, and the reductions of vibration amplitude are 85%.[18] In general, active control requires external input energy to suppress vortex shedding or vortex-induced vibration.

Since passive control is simpler and easier to implement, it is more suitable for engineering applications. Gao *et al.* studied the effects of surface roughness on the VIV response of a flexible structure.[19] They observed that the VIV response reduced, and the vortex shedding frequency increased with the surface roughness. Zhou *et al.* presented the force and flow characteristics of a circular obstacle with the uniform surface roughness.[20] They investigated the surface roughness modeled using different approaches such as grit and net. However, the surface roughness is covered uniformly. Shao *et al.* controlled the flow and vortices around a square cylinder by using an attached flexible plate.[21] Meanwhile, Chen *et al.* studied the vortices and underlying mechanisms according to three circular cylinders aligned in equilateral-triangular arrangements.[22] The VIV response of flexible pipe fitted with helical strakes has been studied, and the main frequency of VIV response was magnified.[23] Ping *et al.* and Qiu *et al.* investigated the effect of diameter difference and mass ratio on the control of two cylindrical VIV vibrations, respectively.[24,25] Through research, Franzini performed the effect of an elastic rotative nonlinear vibration absorber (ERNVA), and the maximum amplitude is decreased by 25%.[26] Based on the studies, changing the wall properties of the structure can suppress the VIV response. The addition of grooves to the surface of an object has also been found to be effective in suppressing the VIV response. Wang *et al.* presented the roughness effect on the aerodynamic characteristics of the cylinder.[27] The spanwise grooves on VIV suppression have been investigated by Law and Jaiman.[28] They found that the maximum cross-flow amplitude and drag decreased considerably compared with that of the general cylinder.

In addition, the bionic structure is also an important reference for developing VIV suppression methods. Observing the structural characteristics of organisms can also bring inspiration to the research on the VIV control method. Wang *et al.* have carried out a series of studies based on the fact that cacti growing in the desert can effectively resist long-term wind.[29] The main focus of the study is on the size of the grooves, and the distribution of the grooves is uniform. The distance between the free surface and the cylinder with ribs was also investigated.[30] Different rib heights had different effects on the VIV response. As the height ratio of the cactus-shaped structure increased, the absolute value of the vortex intensity gradually decreased, and the distance between the vortex shedding location and the cylinder gradually increased. Due to the cactus-shaped structure, the vortex shedding is away from the cylinder, preventing the coupling of wake vortices and effectively suppressing the VIV response.[31] In summary, the addition of cactus ribs to the cylinder is effective in suppressing VIV response. Similarly, is it beneficial to provide random grooves on the surface of a cylinder to suppress its vibrations? This will be discussed in detail in this study.

To systematically study the effect of random grooves, the VIV response of the cylinders with random grooves is investigated numerically based on fluid–structure interaction (FSI) analysis. A description of the problem and the geometrical model of the cylinder with random grooves are presented in Sec. II. The groove coverage ratios (k) are 0%, 15%, 25%, 50%, 75%, and 100%. The numerical method for the VIV response and validation method are given in Sec. III. The effect of groove coverage ratios on VIV suppression is discussed in Sec. IV. Some important conclusions are drawn in Sec. V.

II. PROBLEM DESCRIPTION

The structural characteristics of giant cacti in the desert favor their survival, particularly their resistance to wind.[30,31] Observing the structural characteristics of biological vibration control can shed light on the study of VIV suppression. Similarly, trees can stand effectively in windy environments. The uniform grooves of the cactus cylinder are effective in inhibiting vortex shedding. The rough tree bark has a lot of randomly distributed groove structures of different shapes and sizes. The effect of the random grooves on the tree surfaces is still unclear. This study will investigate the effect of the random grooves using fluid–structure interaction CFD simulations.

The geometry model of the grooved cylinder inspired by rough tree bark is given in Fig. 1 including (a) rough tree bark, (b) cross section of the tree trunk with random grooves, and (c) parameter-setting of the groove and cylinder. Here, the outer diameter of the cylinder is D, and the inner diameter is d. The shape of each small groove is an equilateral triangle, the interior angle of the groove is α, and the central angle of the groove is β. Based on the previous study,[29] $H/D = 0.075$ is

FIG. 1. (a) Rough tree bark, (b) cross section of the tree trunk with random grooves, and (c) parameters of the groove.

TABLE I. Parameters of the groove and cylinder.

Denomination	Symbol	Value
Diameter of the cylinder	D (m)	0.1
Diameter of the inner circle	d (m)	0.085
Interior angle of the groove	α (°)	60
Central angle of the groove	β (°)	10
Height of the groove	H (m)	0.0075
Height ratio of the groove	H /D	0.075
Number of the grooves	N	0, 9, 18, 27, 36
Coverage ratio of the grooves	$K = N/36$	0%, 25%, 50%, 75%, 100%

used in this study since the suppression effect is significant when at 0.075, and further increasing the height, the ratio will not enhance the vibration suppression effect. The parameters of the VIV system are shown in Table I. Figure 2 shows the circular cylinder with a different number of random grooves. The coverage ratio of the random grooves is represented by the letter k. In this paper, $k = 0\%$ ($N = 0$), $k = 25\%$ ($N = 9$), $k = 50\%$ ($N = 18$), $k = 75\%$ ($N = 27$), and $k = 100\%$ ($N = 36$).

The two DOF spring-mass-damping VIV system is used in the study, as shown in Fig. 3, including a cylinder with random grooves, two springs, and two dampers. C is the damping, and K is the spring stiffness. The x-direction is the flow direction, and the y-direction is perpendicular to the flow direction. The mass and natural frequencies are the same in both X and Y directions.

III. NUMERICAL METHOD

A. Vibration equations and Newmark-β method

A combined mass-spring-damper model (Fig. 3) is used to describe the dynamic responses of the cylinder.[32] The two degree-of-freedom vibration equations in the x-direction and y-direction are given in the following equation:

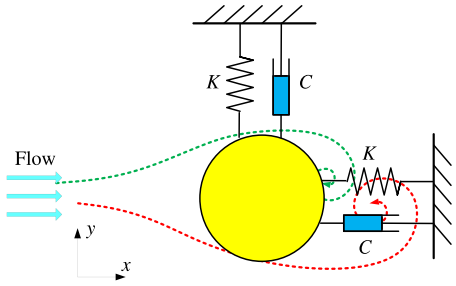

FIG. 3. A schematic of the two-degree-of-freedom VIV system.

$$m\ddot{x} + C_{\text{total}}\dot{x} + Kx = F_{\text{fluid,x}}(t), \tag{1}$$

$$m\ddot{y} + C_{\text{total}}\dot{y} + Ky = F_{\text{fluid,y}}(t), \tag{2}$$

where m is the mass of the cylinder, x and y are the displacements of the cylinder in x-and y-directions, and $F_{\text{fluid,x}}(t)$ and $F_{\text{fluid,y}}(t)$ are the fluid force acting on the cylinder in x-and y-directions. $C_{\text{total}} = 2\xi_{\text{total}}\sqrt{M \cdot K}$ is the total damping of the VIV system.

The Newmark-β method has been widely used to solve differential equations in structural dynamics,[33,34] such as the model described in Eqs. (1) and (2), take cross-flow vibration (in the y-direction) as an example, the displacement y, velocity $\dot{y}$, and acceleration $\ddot{y}$ can be formulated, respectively, as

$$y_{t+\Delta t} = (y_t + \dot{y}\,\Delta t) + \left[\left(\frac{1}{2} - \beta\right)\ddot{y}_t + \beta\ddot{y}_{t+\Delta t}\right]\Delta t^2, \tag{3}$$

$$\dot{y}_{t+\Delta t} = \frac{\gamma}{\beta\,\Delta t^2}(y_{t+\Delta t} - y_t) - \left(1 - \frac{\gamma}{\beta}\right)\dot{y}_t - \left(1 - \frac{1}{2\beta}\right)\ddot{y}_t\Delta t, \tag{4}$$

$$\ddot{y}_{t+\Delta t} = \frac{1}{\beta\,\Delta t^2}(y_{t+\Delta t} - y_t) - \frac{1}{\beta\Delta t}\dot{y}_t - \left(\frac{1}{2\beta} - 1\right)\ddot{y}_t, \tag{5}$$

where the subscript t or $t + \Delta t$ denote the time level. The parameters γ and β are two adjustable weighting constants. According to the

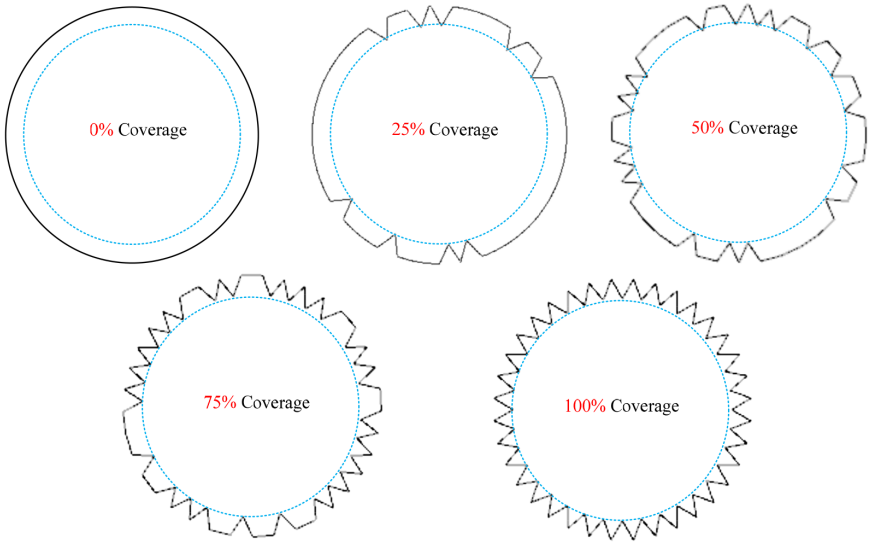

FIG. 2. The cylinder with the different number of random grooves: The groove coverage ratio increases from 0% to 100%.

studies in Refs. 35 and 36, the method is unconditionally stable for $\beta \geq \gamma/2$ and $\gamma \geq 0.5$. The values of γ and β are 0.5 and 0.25, which gave unconditionally stable and second-order accuracy for non-dissipative linear systems.

Considering Eq. (2) at the time $t + \Delta t$, we have

$$M\,\ddot{y}_{t+\Delta t} + C_{\text{total}}\,\dot{y}_{t+\Delta t} + K\,y_{t+\Delta t} = F_{\text{fluid},y}(t)_{t+\Delta t}. \tag{6}$$

The substitution of Eqs. (3)–(5) into Eq. (6) gives

$$[\overline{K}]\,y_{t+\Delta t} = [\overline{F}], \tag{7}$$

where

$$[\overline{K}] = K + \frac{1}{\beta\,\Delta t^2}M + \frac{\gamma}{\beta\,\Delta t}\,C_{\text{total}}, \tag{8a}$$

$$[\overline{F}] = F_{\text{fluid},y}(t)_{t+\Delta t} + \left[\frac{1}{\beta\,\Delta t^2}\,y_t + \frac{1}{\beta\,\Delta t}\,\dot{y}_t + \left(\frac{1}{2\beta} - 1\right)\ddot{y}_t\right] M + \left[\frac{\gamma}{\beta\,[t^2}\,y_t - \left(1 - \frac{\gamma}{\beta}\right)\dot{y}_t - \left(1 - \frac{1}{2\beta}\ddot{y}_t\right] C_{\text{total}}\right). \tag{8b}$$

The developed computer algorithms are employed to solve Eqs. (4), (5), and (7) as this approach has been applied in our study.[37,38]

B. Two-way FSI simulation

In fluid dynamics, VIV is the motion induced on bodies interacting with a flow, which is a typical FSI (fluid–structure interaction) response. In this study, the numerical simulation process for VIV consists of two parts: solving fluid forces and solving vibration equations. The flow chart of the simulation process is presented in Fig. 4.

(1) Obtaining fluid force is the basis of motion simulation. Specifically, CFD software Fluent using the Reynolds-Averaged Navier–Stokes (RANS) equations with the shear stress transport (SST) k–ω turbulence model is adopted in this study.
(2) User-defined functions (UDF) module is used to complete the two-way communication between the fluid force and the motion. The second-order linear differential equation [Eqs. (1) and (2)] is solved based on Newmark-β method. The developed computer algorithms of the Newmark-β method, written with C++, have been embedded in the UDF module. Therefore, the current vibration velocity, displacement, etc., could be obtained. Then, according to the displacement, the new position of the cylinder is transmitted to the CFD solver to update the grid.

C. Computational domain and mesh

The computational domain of the VIV system is given in Fig. 5. The scope of the computational domain is 20D in the cross-flow direction and 40D in the flow direction (D is the diameter of the cylinder). The cylinder is located in sub-domain. The motion of the sub-domain is realized using the layering method (dynamic mesh technology). Slideway is divided into two parts, A and B, which are distributed in the cross-flow and flow directions. According to previous research,[39] the wall effect of the computational domain is negligible when the blocking ratio (D/W, W is the width of the computational domain) is less than 0.05. The blocking ratio is $D/W = 0.05$ in this study. There are four boundary conditions, including inlet, side-wall, outlet, and cylinder-wall. The inlet is velocity-inlet, and the outlet is pressure-outlet. The cylinder-wall is the no-slip wall. To enhance the quality of the mesh, the prism layer around the cylinder is used to improve the calculation accuracy of the boundary layer. The quadrilateral mesh of the computational domain is shown in Fig. 6.

The growth ratio of the boundary layer mesh is 1.05, and the number of layers is 20. The y^+ value of the first layer grid can be calculated by

$$y^+ = 0.721\frac{\Delta y}{D}\text{Re}^{0.9}, \tag{9}$$

where Δy is the height of the first-layer grid, D is the diameter of the cylinder, and Re is the Reynolds number. According to the requests of the k–ω turbulence model, y^+ should be less than 1. Figure 7 shows y^+ values of the cylinder with $U^* = 4$, 10, and 15, in which all the curves are less than 1.0. $U^* = \text{U}/(f_{\text{n,water}}\,D)$ is the reduced velocity (or normalized velocity), and the corresponding Reynolds numbers are 1.58×10^4, 3.96×10^4, and 5.94×10^4 in Fig. 7. Therefore, the quality of the mesh meets the requirements.

D. Numerical method validation

To verify the 2-DOF VIV numerical model, the numerical results are compared with the other experimental and numerical results.[39–41] The VIV system parameters are listed in Table II. Three branches (initial branch, upper branch, and lower branch) can be found and used to describe the VIV response characteristic. In the initial and upper

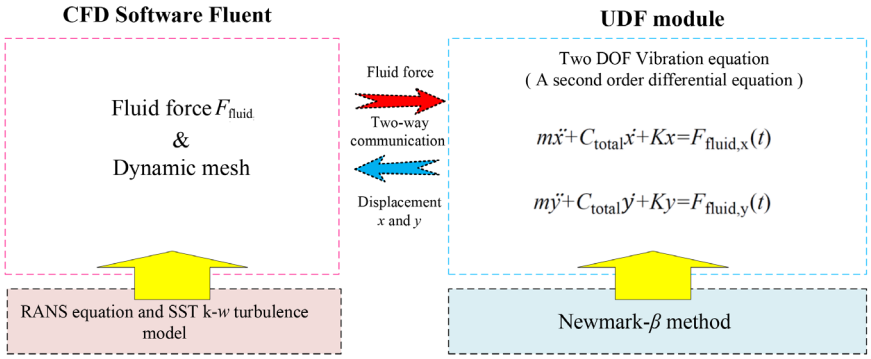

FIG. 4. Two-way FSI simulation process for VIV with the variable damping model.

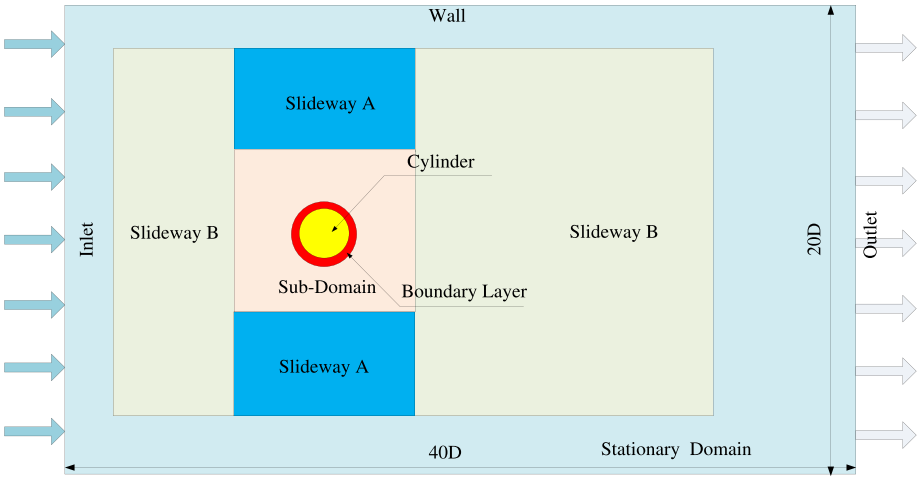

FIG. 5. Computational domain of the VIV system.

branches, the current result is similar to others results in most cases. In addition, the upper branch region is narrower. Although there is some difference between the numerical results and the experimental results, the trend is stable and remains the same as the experimental data. The numerical results in this paper are closer to the experimental results compared to Kang *et al.* In the lower branch, the amplitude ratio of current research results is slightly higher than that of other studies. There are three reasons for this difference. The first reason is that the monitoring conditions of the experiment are limited. Meanwhile, the experiment and simulation cannot maintain the same parameters. The last reason is that the study is based on a two-dimensional model. However, the flow in three-dimensional environment is complex and sensitive. Similar phenomena have been found in other Ref. 42. In addition to that, the numerical results are in accordance with experiment results, so the two-way FSI numerical method is acceptable in most instances (Fig. 8).

IV. RESULTS AND DISCUSSION

A. VIV amplitude and frequency responses

The cross-flow amplitude ratios (A_y^*) of the cylinder with random grooves and vortex shedding frequency ratios (f_y^*) are given in Figs. 9 and 10. The vortex shedding frequency is calculated by fast Fourier transform (FFT). The lock-in phenomenon occurs when the vortex

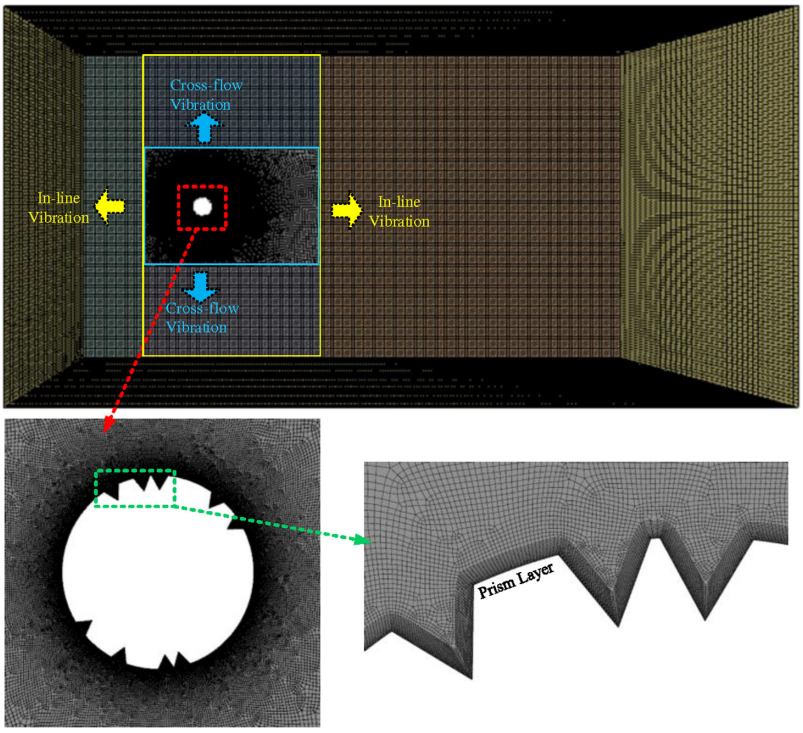

FIG. 6. Mesh of the computational domain, mesh near the boundary layer, and mesh near the grooves.

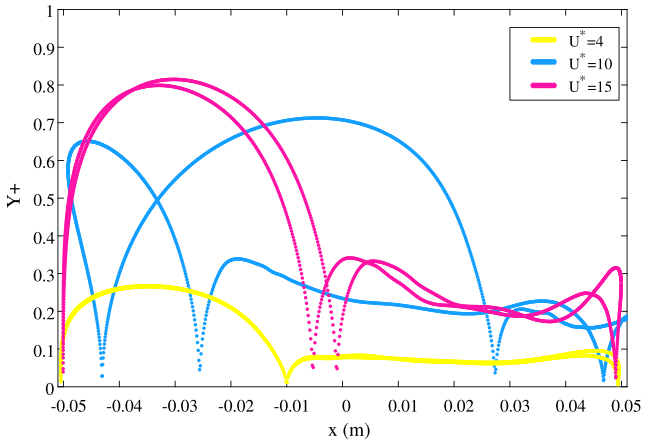

FIG. 7. Y+ values of the cylinder walls with $U^* = 4$, 10, and 15.

TABLE II. The parameters of the 2-DOF VIV system.

Denomination	Symbol	Value
Diameter of the cylinder	D (m)	0.1
Mass of the cylinder	m (kg)	20.42
Mass-ratio	m^*	2.6
Added mass coefficient	C_{add} (N/(m/s))	1.0
Natural frequency in water	$f_{n,water}$ (Hz)	0.4
Spring stiffness	K (N/m)	179
Damping-ratio	ξ_{total}	0.005

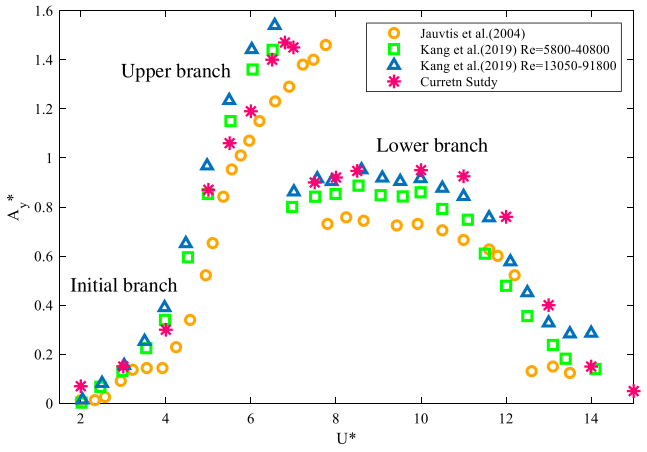

FIG. 8. Comparison of the numerical results from the current study and the other results from Jauvtis *et al.*[40] and Kang *et al.*[41] for the VIV amplitudes at $m^* = 2.6$ and $\xi = 0.005$.

shedding frequency is close to the natural frequency. In Fig. 9, four branches are usually used to identify the VIV response region, including the initial branch, upper branch, lower branch, and desynchronization region.

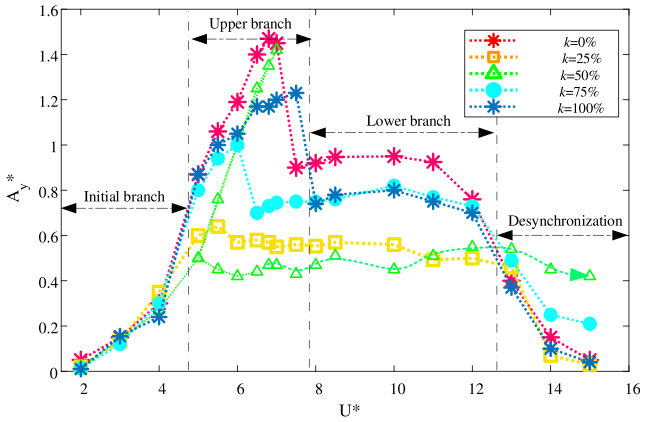

FIG. 9. The amplitude responses of the grooved cylinders with different coverage ratios.

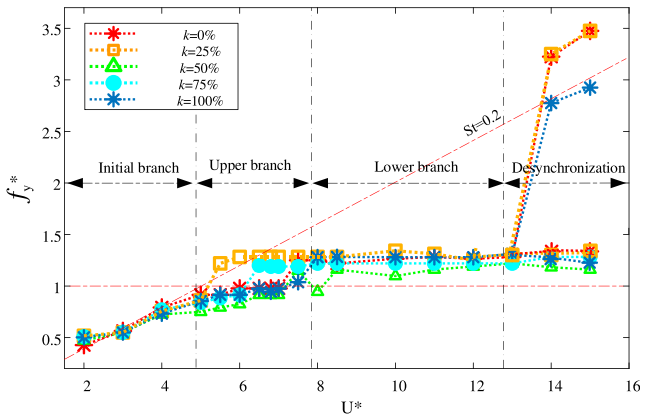

FIG. 10. The frequency responses of the grooved cylinders with different coverage ratios.

In the initial branch region, the VIV responses with different groove coverage ratios ($k = 0\%$, $k = 25\%$, $k = 50\%$, $k = 75\%$, and $k = 100\%$) are characterized by the low-frequency ratio and low amplitude ratio. The frequency ratios of all coverages are less than 1.0, which means that it is far away from the resonance frequency. Consequently, the cross-flow amplitude ratios are relatively low and less than 0.4.

In the upper branch region, the cross-flow amplitude ratios of $k = 0\%$, $k = 75\%$, and $k = 100\%$ begin to increase rapidly before the peak value is reached. The peak value of the cross-flow amplitude ratio of $k = 0\%$ is about 1.5. The amplitude ratios of $k = 75\%$ and 100% are about 1.0 and 1.22. The maximum cross-flow amplitude ratio of $k = 25\%$ is reduced by 56.7% when compared with $k = 0\%$. However, the vibration of $k = 50\%$ is unstable. Its peak is 1.5, and another branch value is only 0.5. The vortex shedding frequency ratios of $k = 0\%$ and $k = 100\%$ gradually increase, and they are stable around 1.0. The vortex shedding frequency ratios of $k = 25\%$ and $k = 75\%$ are slightly higher and close to 1.4 and 1.3. In addition, the frequency ratio of $k = 50\%$ is always less than 1.0 in the upper branch.

In the lower branch region, all vibration responses are relatively stable. The vortex shedding frequency ratios of all cases are stable at

about 1.2–1.4, and the cross-flow amplitude ratios are also stable. When $U^* = 11.0$, the cross-flow amplitude ratio of $k = 0\%$, 75%, and 100% begin to decrease. When $U^* = 10.0$, the cross-flow amplitude ratio of $k = 25\%$ begins to decrease. There is a difference, when $U^* = 10.0$, the cross-flow amplitude ratio of $k = 50\%$ keeps stable and even begins to increase.

In the desynchronization region, the VIV responses of all cases are characterized by the low amplitude ratio except $k = 50\%$, which means that the amplitude responses are suppressed in the high Reynolds number region. The vortex shedding frequency ratios of $k = 0\%$, 25%, and 100% are high, and others are lower. For the cylinder with $k = 50\%$, the high amplitude and the frequency response indicate the onset of the galloping response.

B. Vortex phases and estimated vortex shedding patterns

To further understand the relationship between vortex pattern and vortex shedding frequency, the vortex phase (Φ) is introduced.[39,41] The vortex pattern also varies with their phase difference. The relationship between vortex phase and vortex shedding frequency ratio can be expressed as

$$\tan(\Phi) = \frac{2\xi f_{vortex}/f_{n,water}}{1 - \left(f_{vortex}/f_{n,water}\right)^2}. \quad (10)$$

The vortex phases of the grooved cylinder with different coverage ratios are shown in Fig. 11. The vortex pattern is the 2S mode in the initial branch. The 2S mode means that two single vortices shed within one vibration period. The jump of the vortex shedding frequency f_{vortex} occurs in the upper branch (Fig. 11), so the transition from the 2S mode to the P + S or 2P mode occurs in this region. P + S indicates that a pair of vortices shed from one side of the cylinder, and one single vortex sheds from the other side of the cylinder in one cycle. In addition, the 2P mode presents two pairs of vortices shed from each side of the cylinder in one cycle. Wang *et al.* also reported a similar conclusion.[39] More specifically, when the vortex shedding frequency ratio is higher than 1.0, the vortex pattern changes from the 2S mode to the P + S or 2 P mode. At the same time, the vortex phase changes from about 0° to about 180°. Consequently, the vortex phase can be used to predict vortex patterns indirectly. So, in short, close to 180° represents P + S or 2P modes, and close to 0° represents 2S modes. For the cases of $k = 25\%$, 50%, 75%, and 100% coverages, the jump point increases with the groove coverage ratio. It obviously can be concluded that the smaller the number of grooves, the earlier the phase jump.

C. VIV responses and flow structures in different branches

To further understand the fluid characteristics of the smooth cylinder and the cylinder with random grooves, the cross-flow amplitude ratio, lift coefficient, vortex contours, and vortex patterns are further analyzed in this section. Four typical normalized velocities ($U^* = 3.0$, 6.8, 10.0, and 13.0) are selected to further analyze the VIV responses of the four branch regions.

1. Initial branch

In the initial branch, Fig. 12 shows the time histories of VIV responses of the cylinders with different groove coverage ratios ($k = 0\%$, 25%, 50%, and 100%) when U^*=3.0. Figure 13 shows the vortex contours and vortex patterns. When $U^* = 3.0$, the cross-flow amplitude ratios in the y direction are about 0.15 for all cases. In addition, the amplitude of the 25% coverage ratio shows an unstable vibration response. Similarly, vibration instability is observed for the 50% coverage ratio cylinder in 40–80 s. All the main frequencies are close to each other. The main frequencies of the lift coefficient and cross-flow amplitude are concordant, which is one of the characteristics of the 2S mode. In Fig. 13, the distribution laws of the vortex contours

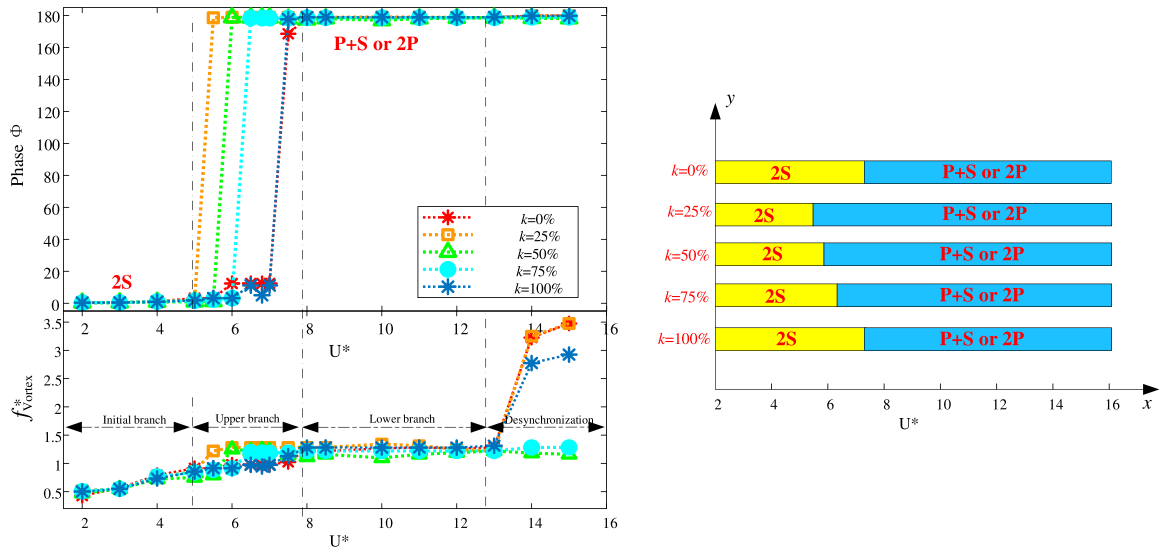

FIG. 11. Vortex phases of the cylinders and vortex patterns.

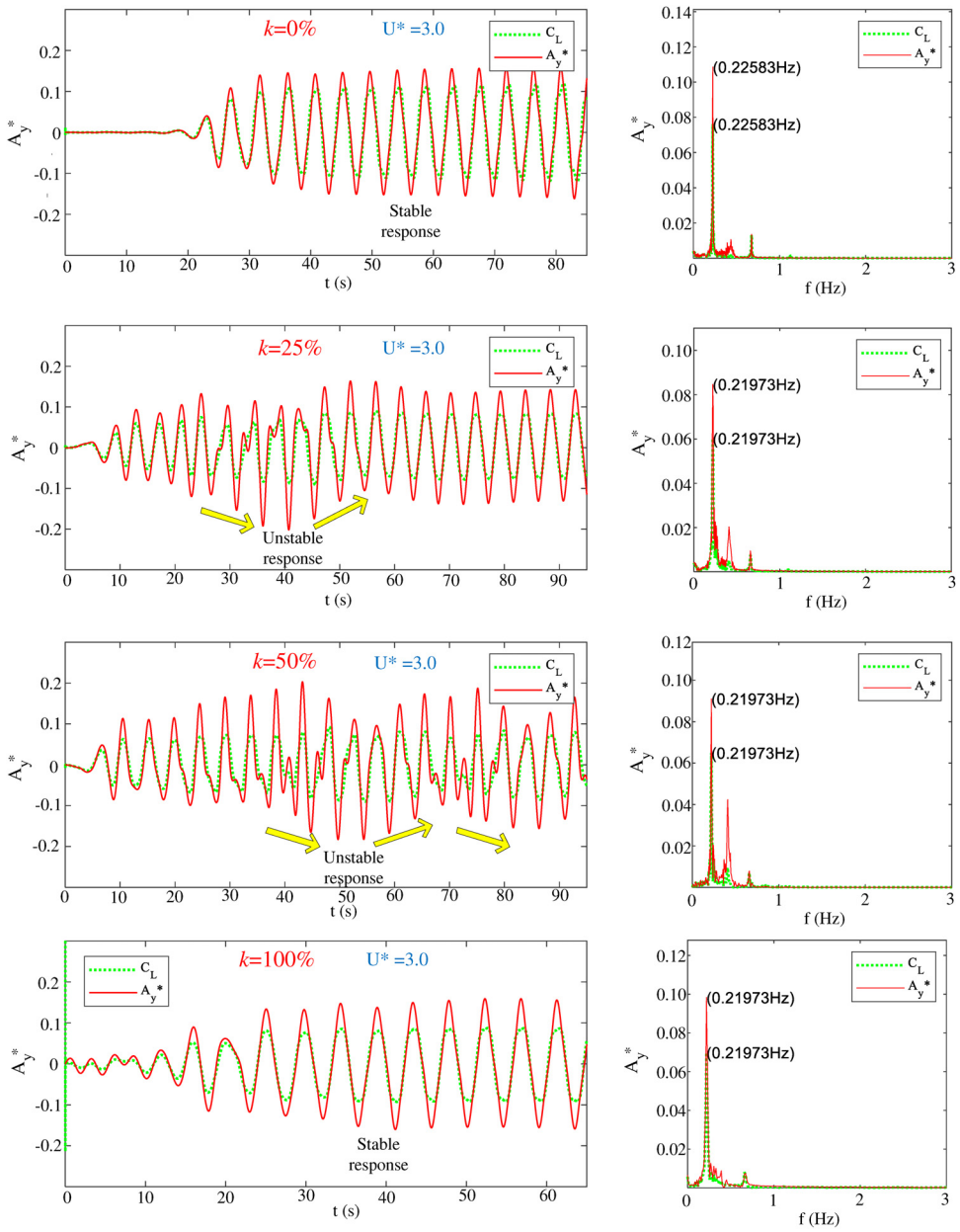

FIG. 12. The time histories of VIV responses of the cylinder with the different number of grooves ($U^* = 3.0$).

are similar to each other. The vortex patterns of all cases are the 2S modes. The rotation directions of the two vortices are opposite. In the initial branch, the 2S mode is similar to the phenomenon of Karman vortex street, which has been observed in the experiments.[41]

2. Upper branch

In the upper branch, Fig. 14 shows the time histories of the VIV response of the grooved cylinder with different coverage ratios ($k = 0\%$, 25%, 50%, and 100%) when $U^* = 6.8$. The vortex contours and vortex patterns are given in Fig. 15. The amplitudes in the upper region for all cases are higher than the initial region. When $U^* = 6.8$, the peak value of the amplitude ratio for $k = 0\%$ and $k = 50\%$ in the y direction is about 1.5. The peak value of the amplitude ratio for $k = 25\%$ is about 0.7, which is reduced by 41.7% compared with that of 0% coverage. The peak value of the amplitude ratios for 100% is about 1.2. The cylinder with the 50% coverage ratio shows an unstable vibration with an increase in amplitude ratio at 60 s. In general, the motion becomes stable when the vortex shedding frequency resonates with the natural frequency. The unstable vibration phenomenon is

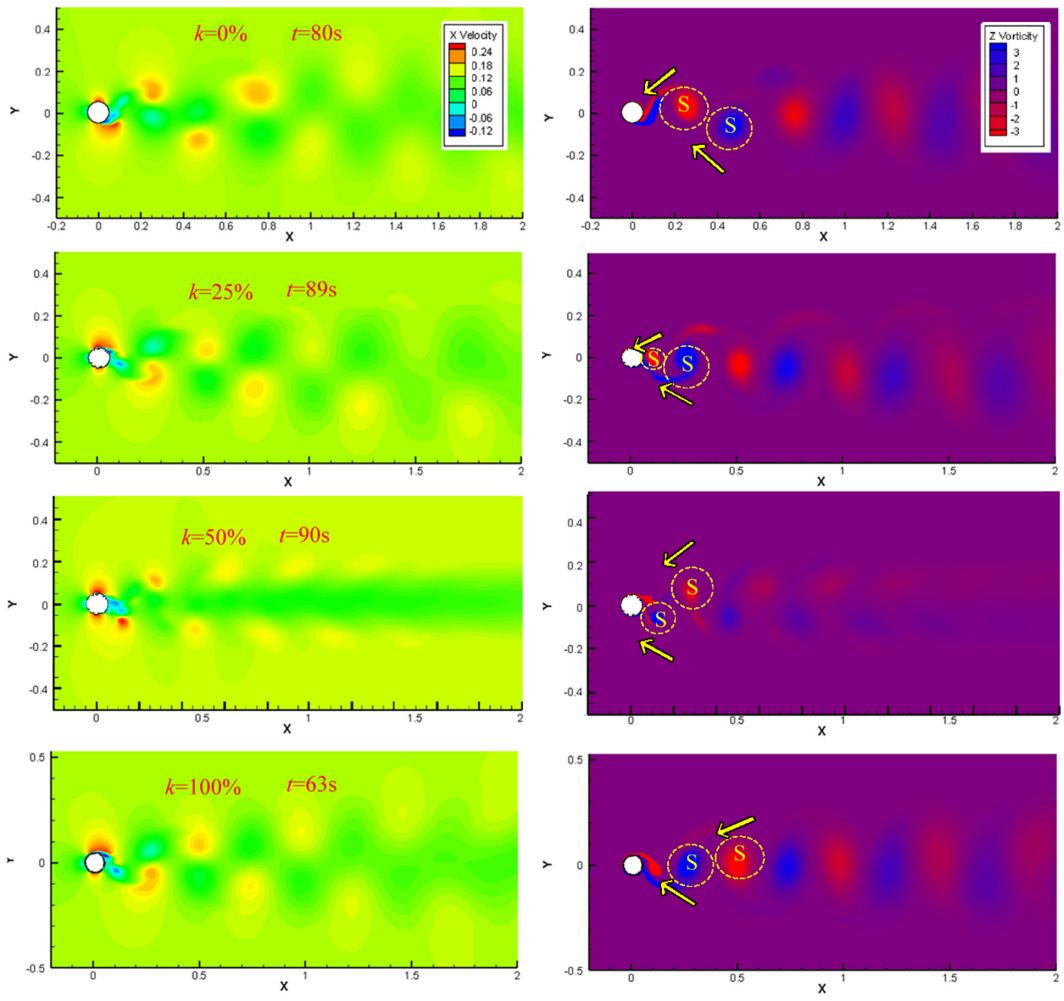

FIG. 13. The vortex contours and vortex patterns of the cylinder with the different number of grooves ($U^* = 3.0$).

caused by the instability of vortex shedding, since the vortex shedding frequency of $k = 50\%$ does not match the natural frequency in some cases. The cylinder enters large amplitude vibration again. This phenomenon is common in the upper branch of the cylinder with $k = 50\%$. This reason is presumed to be due to the excessive number of grooves, resulting in the WIV response approaching the cylinders with $k = 70\%$ and $k = 100\%$.

The main frequencies of lift coefficient and amplitude ratio of the cylinder with 0% groove coverage ratio are the same (0.390 63), which is also the main feature of VIV. The main frequencies of 25% and 100% are 0.5127 Hz and 0.378 42 Hz. For the cylinder with the 50% coverage ratio, due to the unstable vibration, two different peaks (0.3662 and 0.494 38 Hz) of the frequency appear. In Fig. 15, the vortex pattern is the 2S mode for $k = 0\%$ and $k = 100\%$. The vortex patterns of $k = 25\%$ and $k = 50\%$ are the P + S mode. The P + S mode is caused by a series of small vortices generated by the random grooves. The small vortices gradually merge into the large vortices when they leave the wall. Since the random grooves are asymmetric, the vortices on both sides of the cylinder are also asymmetric, which is the reason for the P + S mode. By the way, the P + S mode also appears in other conditions, such as the lower branch of VIV and galloping.

3. Lower branch

In the lower branch, Fig. 16 shows the time histories of the VIV response of the grooved cylinder with different coverage ratios ($k = 0\%$, 25%, 50%, and 100%) when $U^* = 10.0$. The vortex contours and vortex patterns are presented in Fig. 17. When $U^* = 10.0$, the cross-flow amplitude ratio of $k = 0\%$ in the y direction is about 1.0. The cross-flow amplitude ratio of $k = 25\%$ is about 0.55, which is reduced by $k = 50\%$ when compared with $k = 0\%$. Meanwhile, the amplitude ratio of $k = 50\%$, which is about 0.43, is also less than 25%. It is also found that the amplitude ratio curve is asymmetric. As the coverage ratio increases, the cross-flow amplitude ratio of 100%

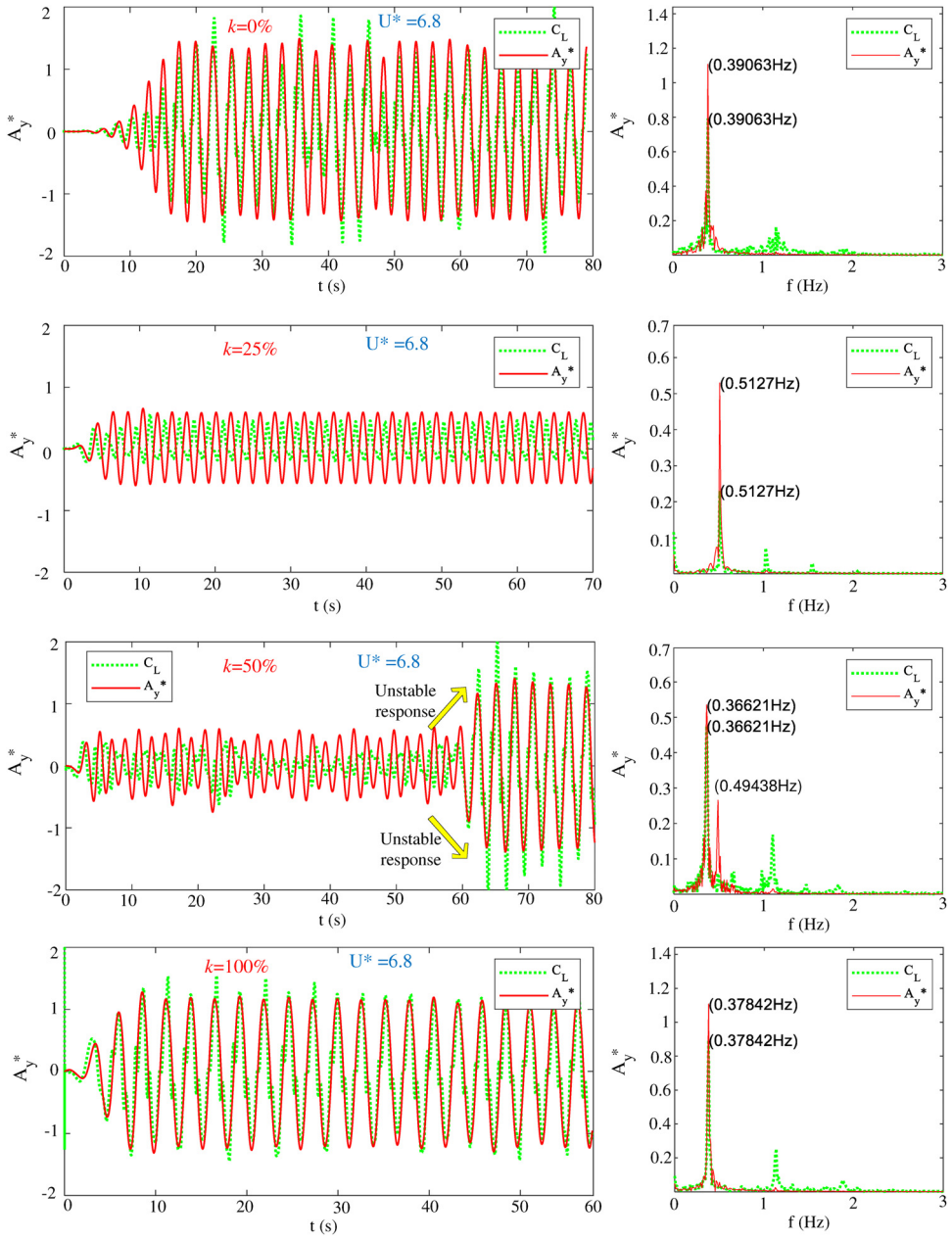

FIG. 14. The time histories of VIV responses of the cylinder with the different number of grooves ($U^* = 6.8$).

reaches 0.75. The dominant frequencies of the cross-flow amplitude ratio of 0%, 25%, and 100% are all close to the natural frequency. However, two peaks occur on the frequency curves when the coverage ratio k is 50%. The main frequency is only 0.439 45 Hz. The secondary frequency is 0.8789 Hz, which is twice as high as the main frequency. In Fig. 17, the vortex patterns of the cylinder with 0%, 25%, and 50% coverage ratios are typical 2 P modes. The vortex pattern of 100% is the P + S mode, which is significantly different from 25% and 50%. The P + S mode is similar in shape to the 2P model of 0%. The difference is the large red vortex of the S mode looks like two undivided vortices.

4. Desynchronization

In the desynchronization region, Fig. 18 shows the time histories of VIV responses of the grooved cylinder with different coverage ratios ($k = 0\%$, 25%, 50%, and 100%) when $U^* = 13.0$. Figure 19 shows the vortex contours and vortex patterns. When $U^* = 13.0$, the cross-flow

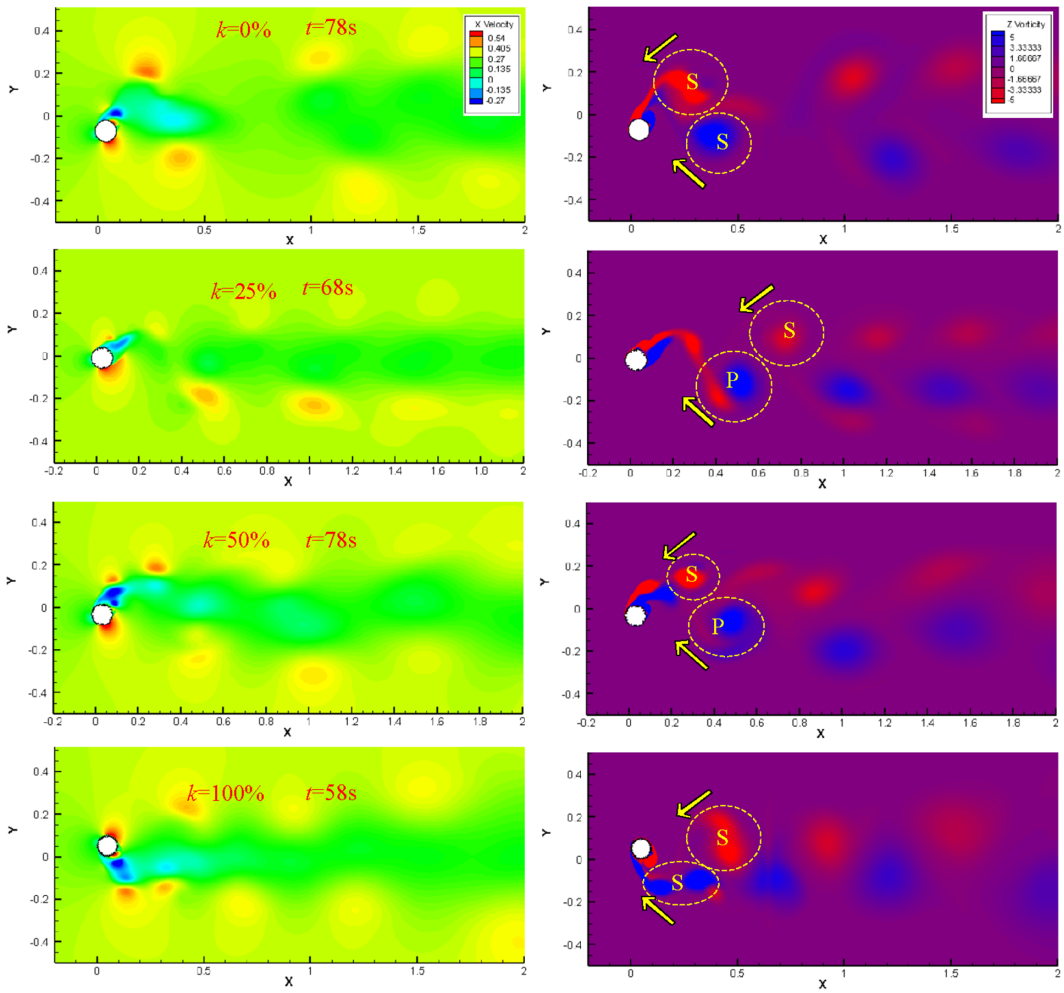

FIG. 15. The vortex contours and vortex patterns of the cylinder with the different number of grooves ($U^* = 6.8$).

amplitude ratio of 0% and 25% in the y direction are about 0.4 and 0.41, respectively. The amplitude ratios of $k = 50\%$ are about 0.53. However, the amplitude ratio of 50% becomes more irregular than that of $k = 25\%$, and it is speculated that the vibration instability is caused by the increase in random grooves and vortices. The amplitude ratio of 100% is only 0.39 and slightly lower than others. The main frequencies of the lift coefficient and the amplitude ratio of 0% are all 0.5127. However, the main frequencies of the lift coefficient and the amplitude ratio of $k = 25\%$, 50%, and 100% do not overlap, which means that the vibration frequency and vortex shedding frequency are not synchronized due to the influence of the random grooves, which is also a characteristic of galloping. In general, the galloping phenomenon may occur in the high flow velocity for a non-circular cross section cylinder. The vortex contours and the vortex patterns of all cases are in the 2P mode (Fig. 19), which is the typical feature of the lower branch and the desynchronization region.

B. In-line VIV amplitude responses and trajectories with two degrees of freedom

The in-line amplitude ratios of the circular cylinders in the x direction are presented in Fig. 20. In the initial branch, the in-line amplitude of 0%, 25%, 50%, and 100% increases first and then decreases with the increase in flow speed. The amplitude of 75% increases continuously. The maximum in-line amplitude ratio for all cases is about 0.1 in the initial branch. In the upper branch, the amplitude ratio keeps increasing after reaching the highest value. The maximum in-line amplitude ratios of 0% and 50% are similar (0.28 and 0.3). Then, the amplitude ratio of 0% and 50% coverage ratio begin to decrease. The maximum in-line amplitude ratios of 75% and 100% are 0.21 and 0.23, respectively. For the coverage ratio of 25%, the amplitude increases slowly, and the maximum amplitude ratio is only 0.13. Therefore, random grooves also have a significant effect on VIV suppression in the x direction when in the upper branch.

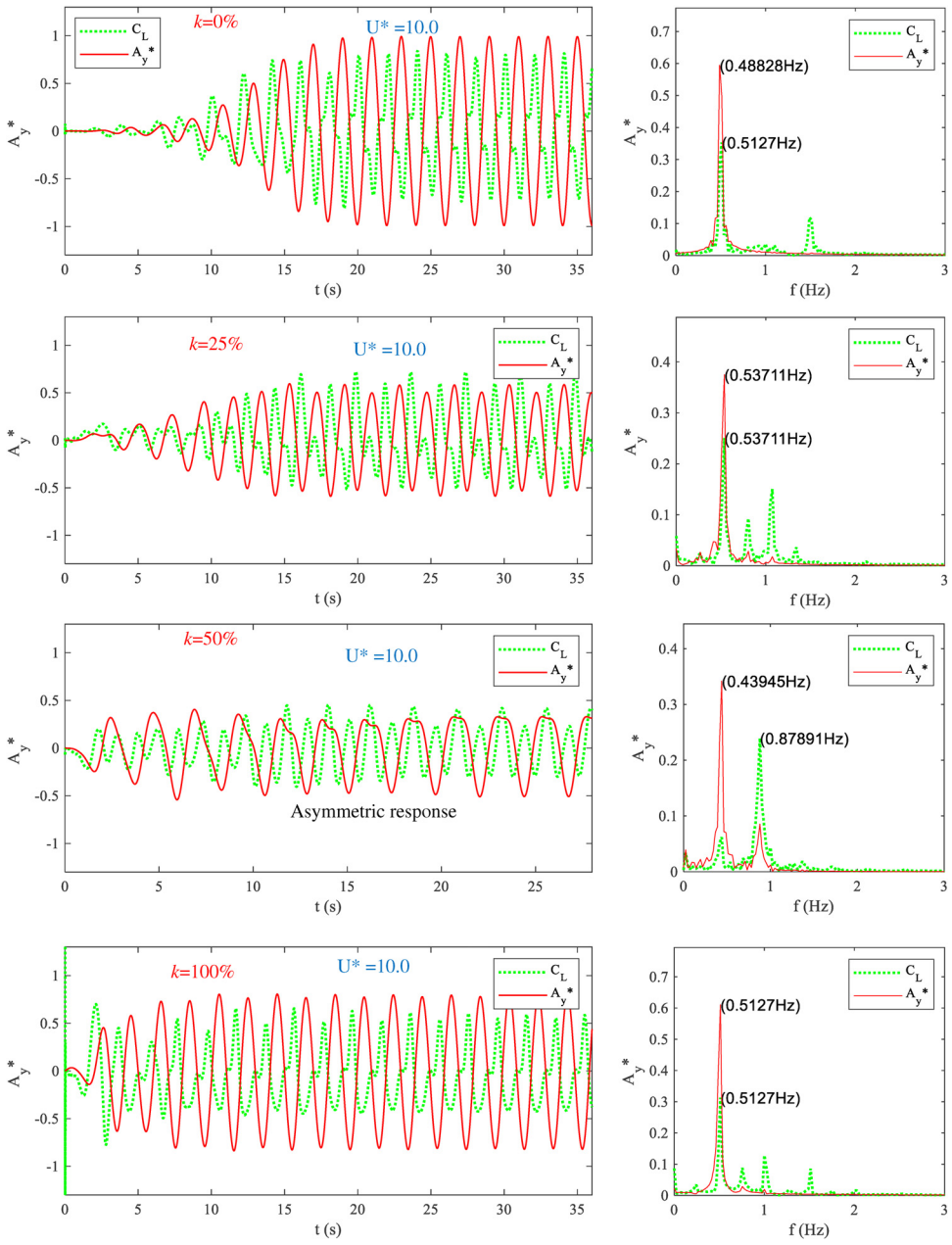

FIG. 16. The time histories of VIV responses of the cylinder with the different number of grooves ($U^* = 10$).

In the lower branch, the in-line amplitude ratios of all cases keep decreasing. The ranges of in-line amplitude ratios of 50% and 75% are about 0.07–0.1. Other amplitude ratios are relatively low 0–0.05. In the desynchronization region, the in-line amplitude ratios of $k = 0\%$, 25%, and 100% continue to decrease until close to 0. The minimum in-line amplitude ratios of 50% and 75% are 0.04 when $U^* = 15$, which are higher than the smooth cylinder (0% coverage ratio). It indicates that the random groove will enhance the in-line amplitude response when in the lower branch and the desynchronization region.

The effects of the random grooves on the in-line amplitude and cross-flow amplitude are different. In general, the vibration caused by vorticity is mainly cross-flow vibration, and the source of in-line vibration is mainly affected by the impact of flow and the nature of the cylinder itself. The random grooves mainly break the large vortex to suppress the cross-flow vibration and indirectly impede the in-line vibration. With Figs. 9 and 20, it can be found that the suppression effect of random grooves is more obvious for cross-flow vibration, but it is also effective for in-line vibration. For Fig. 9, disregarding the

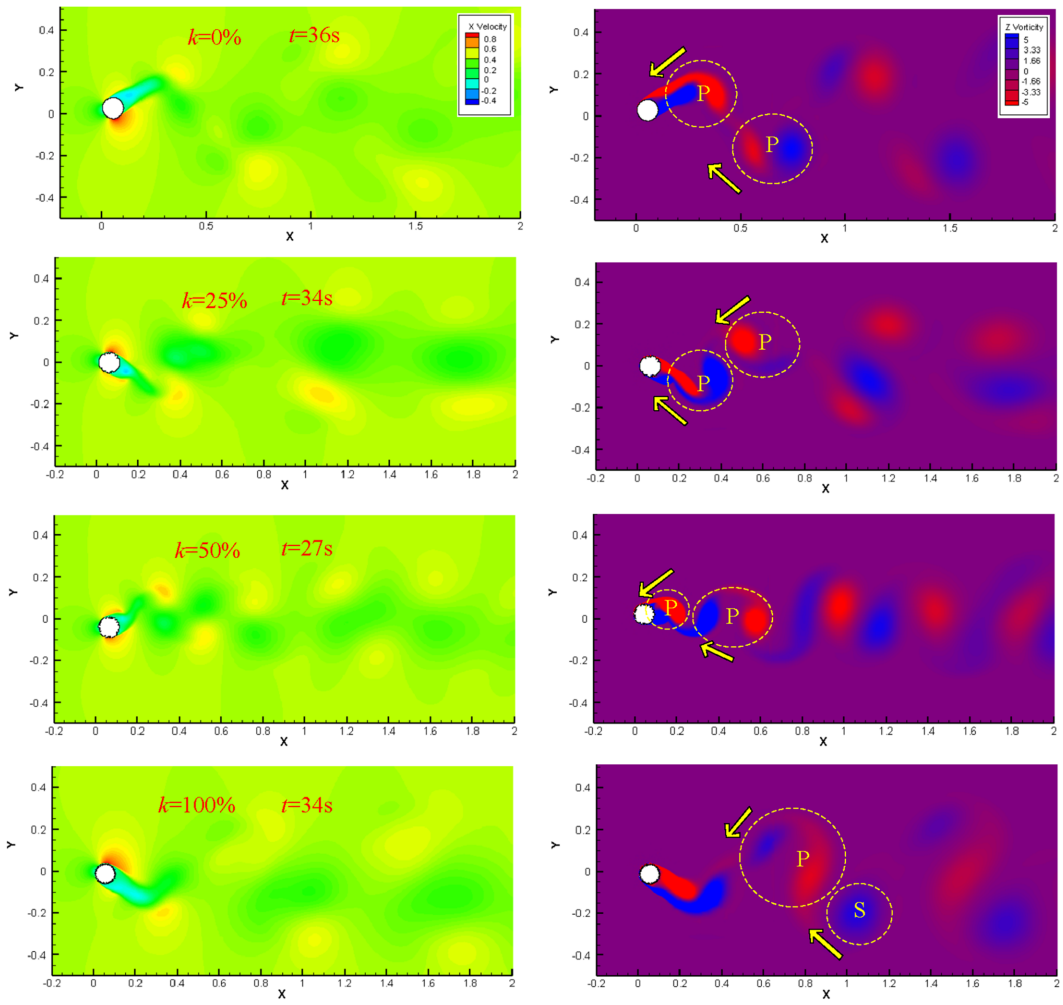

FIG. 17. The vortex contours and vortex patterns of the cylinder with the different number of grooves ($U^* = 10$).

bifurcation of the curve for k = 50%, the cross-flow amplitude ratio for k = 25% is significantly smaller than the other coverage ratios in the upper and lower branches. Meanwhile, the in-line amplitude ratio of k = 25% is also smaller than the other coverage ratios in the upper branch. However, the suppression effect of k = 100% for the in-line vibration is significantly better than the other coverage ratios in the lower branch and desynchronized branch regions. At k = 25%, the suppression effect of cross-flow vibration has a better advantage in most of the reduce velocities. However, different branches correspond to different coverage ratios for the in-line vibration.

The 2-DOF vibration trajectories of the cylinder with random grooves are compared in Fig. 21. For the cylinder with 0% coverage ratio (the smooth cylinder), the vibration trajectory is the typical "8," which is a feature of the 2-DOF VIV response. The range of the trajectory first increases and then decreases with the increase in the reduced velocity. When U^*=3.0, the range of vibration trajectory is very small ($-0.02\,\text{m} < A_y < 0.02\,\text{m}$; $-0.002\,\text{m} < A_x < 0.02\,\text{m}$). When $U^* = 6.5$, the range of vibration trajectory is the biggest ($-0.15\,\text{m} < A_y < 0.15\,\text{m}$; $0.02\,\text{m} < A_x < 0.08\,\text{m}$). Then, the range of trajectory starts to decrease. In particular, the trajectory shapes in different branches are summarized in Fig. 22. They are similar to the research reported by Jauvtis *et al.*[40]

For the cylinder with the 25% coverage ratio, the vibration trajectory is no longer like an "8" when $U^* > 6.5$. The asymmetrical trajectory of 25% shows an inverted raindrop shape when $U^* = 6.5$ and $U^* = 10.0$. The random grooves lead to asymmetrical vortices and further lead to asymmetrical trajectories. Compared to the cylinder with the 0% coverage ratio, the amplitude ratio of 25% is significantly lower, which means that the vibration response has been significantly suppressed.

For the cylinder with the 50% coverage ratio, the vibration trajectory is unstable when $U^* = 6.5$, and the range of trajectory is $-0.12\,\text{m} < A_y < 0.12\,\text{m}$ and $0.02\,\text{m} < A_x < 0.1\text{m}$. Similar phenomena have been found in Fig. 14 in the upper branch, which indicates the effects of random grooves with the 50% coverage ratio have instability. The trajectory of 50% looks like the top half of a hamburger bun.

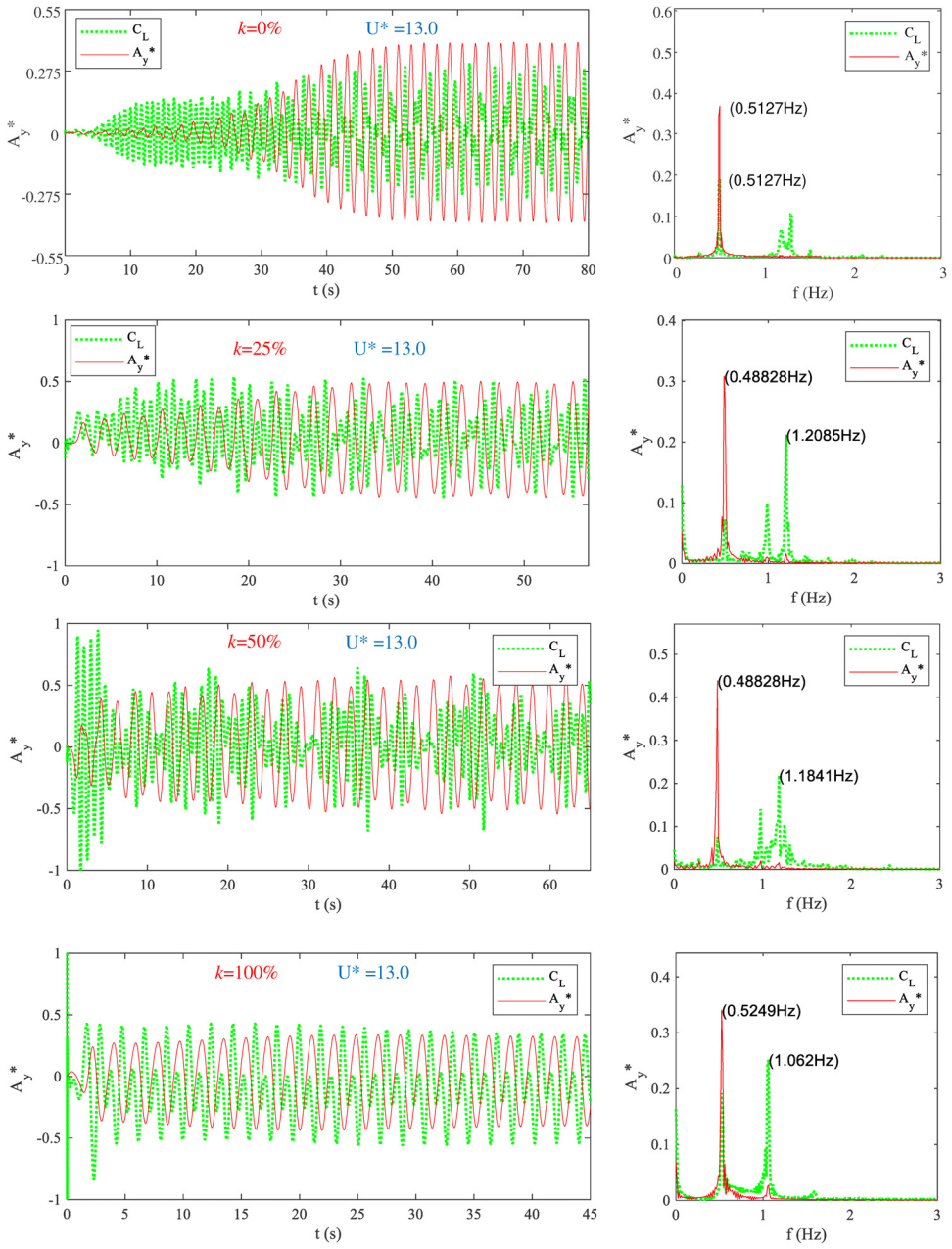

FIG. 18. The time histories of VIV responses of the cylinder with the different number of grooves ($U^* = 13.0$).

For the cylinder with the 75% coverage ratio, the vibration shows a typical "8" trajectory at $U^* = 3$ and 6.5. For other cases, the vibration trajectory is like the number "1." In addition, the amplitude of 75% is still less than the smooth cylinder (0% coverage ratio).

For the cylinder with the 100% coverage ratio, the vibration trajectory is also like the number "8" when $U^* = 3.0$, 5.0, 6.5, and 10.0. In particular, the trajectory of a 100% coverage ratio is similar to the trajectory of the smooth cylinder (0%).

V. DISCUSSION ON THE VIV SUPPRESSION MECHANISM

A. Pressure distribution on the cylinders

The impact mechanism of the random grooves on the VIV response can be obtained by analyzing pressure distribution around the cylinder. The cases with k = 50% and 75% are not representative. The pressure contours and pressure distributions of k = 0%, k = 25%, and k = 100% are the most representative and adopted to investigate

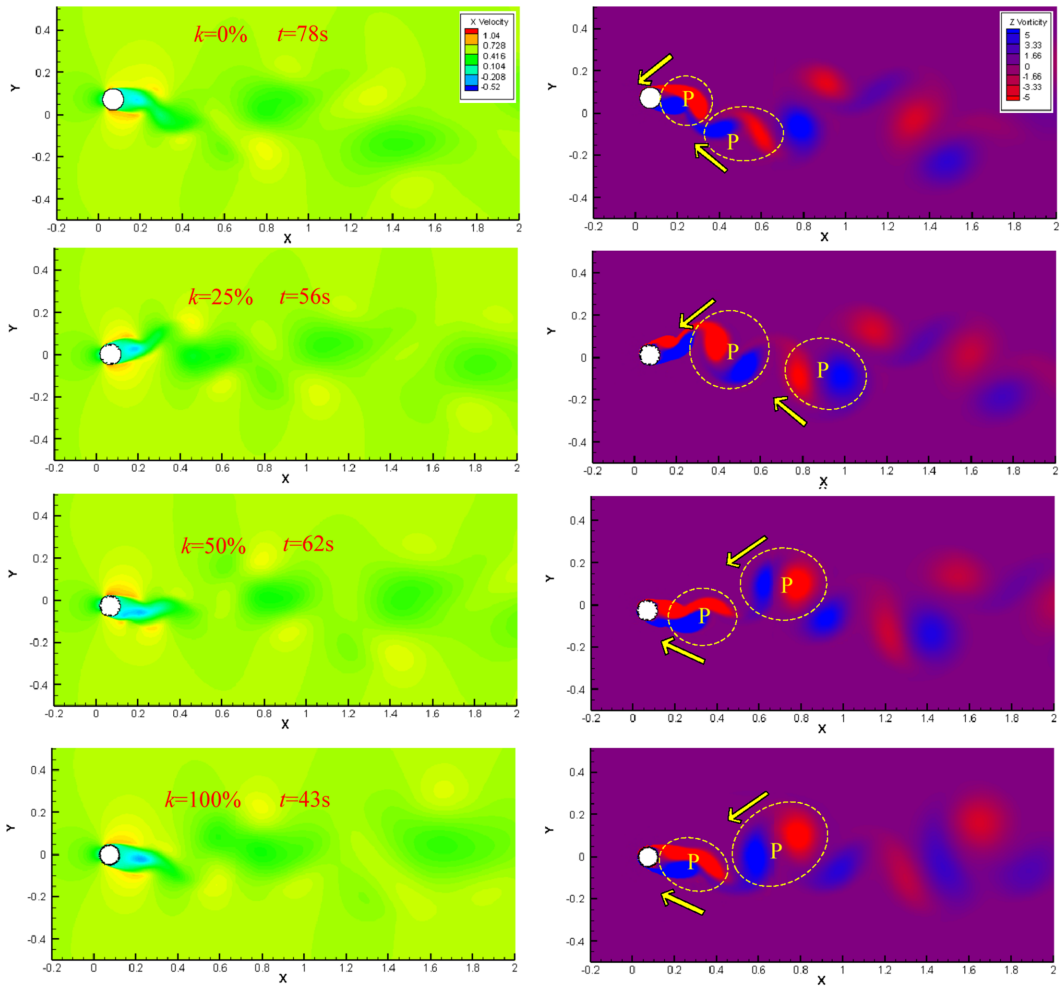

FIG. 19. The vortex contours and vortex patterns of the cylinder with the different number of grooves ($U^* = 13.0$).

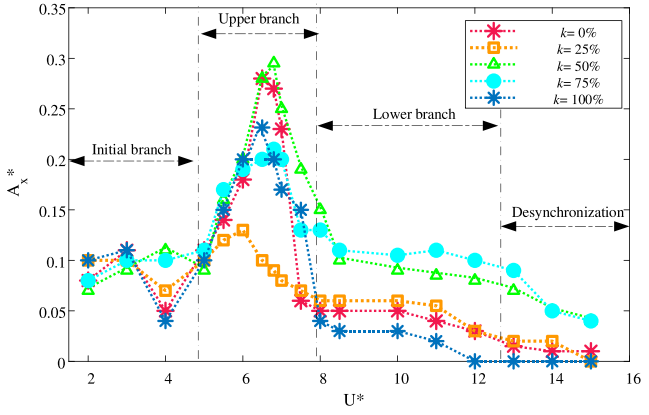

FIG. 20. The in-line amplitude responses of the circular cylinders with different random grooves.

the VIV suppression mechanism of a small number of grooves, as shown in Fig. 23. The cylinders are all approaching the highest point of the vibration trajectory. The pressure distributions around the cylinders with $k = 0\%$ and $k = 100\%$ are very similar, which means they have similar vibration responses. A high-pressure region is observed at the lower left side of the cylinder. A low-pressure region is observed at the lower right side of the cylinder. In addition, a secondary low-pressure region is observed at the upper side of the cylinder. For the cylinder with the coverage ratios of $k = 25\%$, the pressure contour is different. The high-pressure region on the lower side of the cylinder is relatively small. More specifically, due to the random grooves ($k = 25\%$), some small-scale vortices are generated and change the development of the main vortices, and thereby affect the pressure distribution. Consequently, the high-pressure region next to the random grooves on the lower side of the cylinder disappear.

Pressure distributions on the cylinders from Fig. 23 are compared in Fig. 24 using polar coordinates. In general, the pressure on the lower

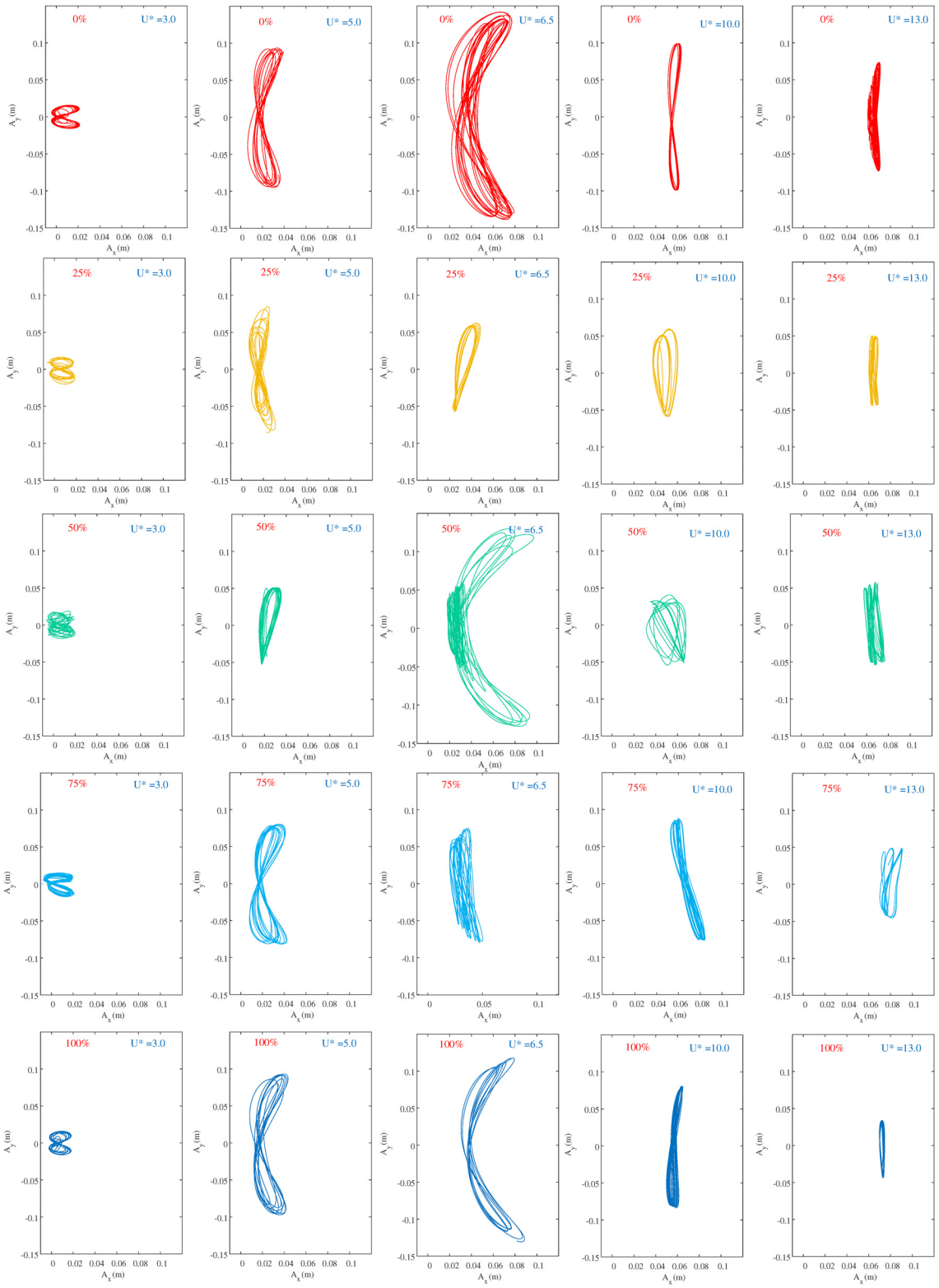

FIG. 21. The trajectories of the circular cylinder with random grooves.

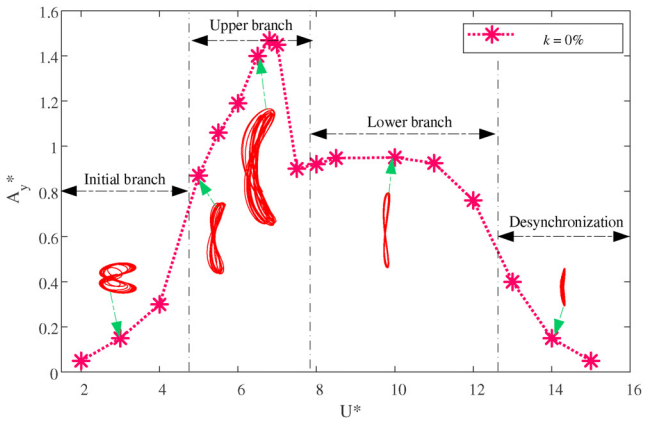

FIG. 22. Trajectory shapes in different branches.

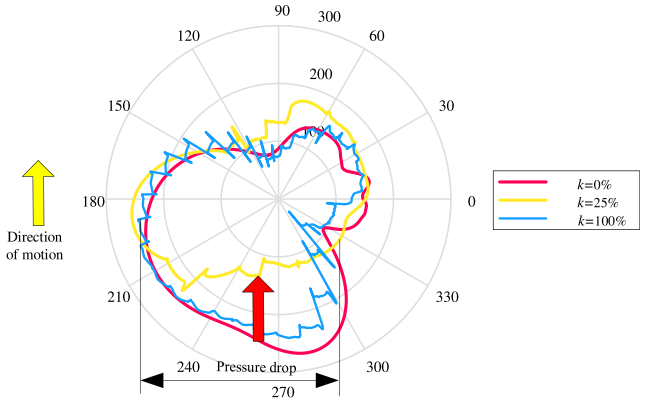

FIG. 24. Pressure distribution on the cylinders when approaching the highest point of vibration.

side of the cylinder is larger, while the pressure on the upper side is smaller, so the direction of the resultant force is upward. The pressure distributions of the cylinders of 0% and 100% have similar distribution patterns. The difference is that the high-pressure region of the smooth cylinder (0%) is stronger. In contrast, the pressure values on the cylinder with $k = 25\%$ are relatively low. Specifically, in the interval of 210°–310°, a significant pressure drop can be observed. The disappeared high-pressure region has also been marked in Fig. 23. This indicates that random grooves on the lower side of the cylinder generate a series of small vortices and suppress the formation of high-pressure regions. As a result, the resultant force in the direction of motion is significantly reduced. This explains why a small number of random grooves (such as $k = 25\%$ and 50%) can suppress vibration.

B. Flow structure around the cylinders

The vorticity contours around the cylinder when approaching the highest point and the middle point of the vibration trajectory are given in Fig. 25. For the vortex distribution of $k = 0\%$, since the boundary layer separation occurs on the upper and lower sides of the cylinder, there are two shedding vortices, and the rotation directions

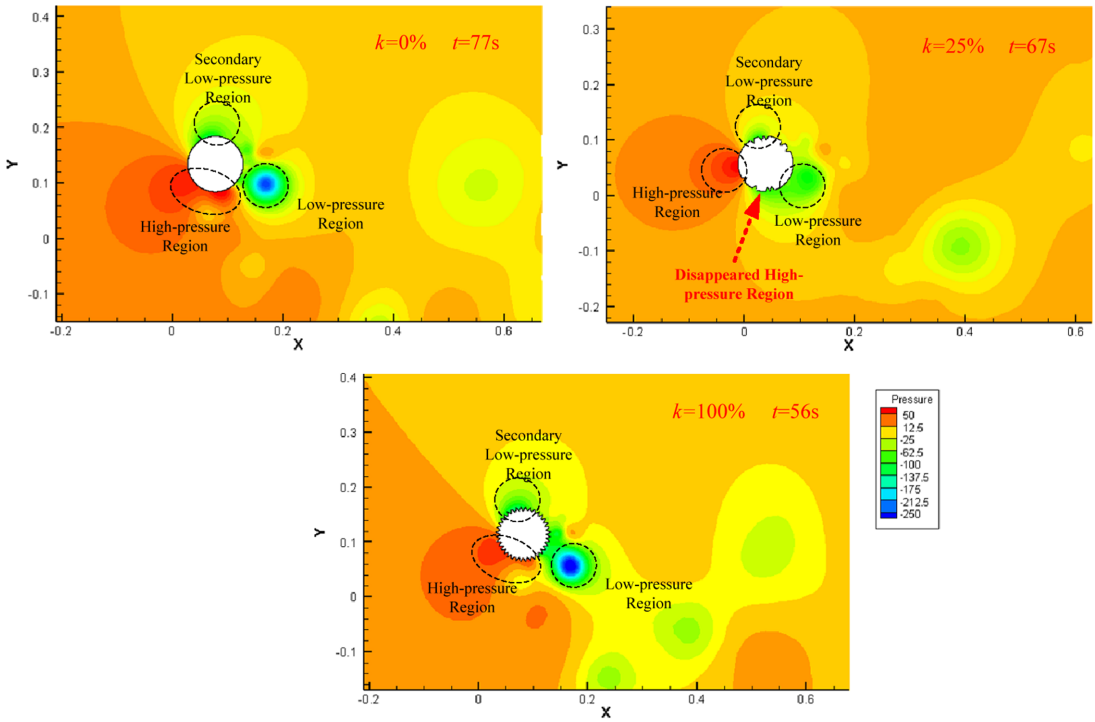

FIG. 23. The pressure contours around the cylinders with random grooves at $U^* = 6.8$.

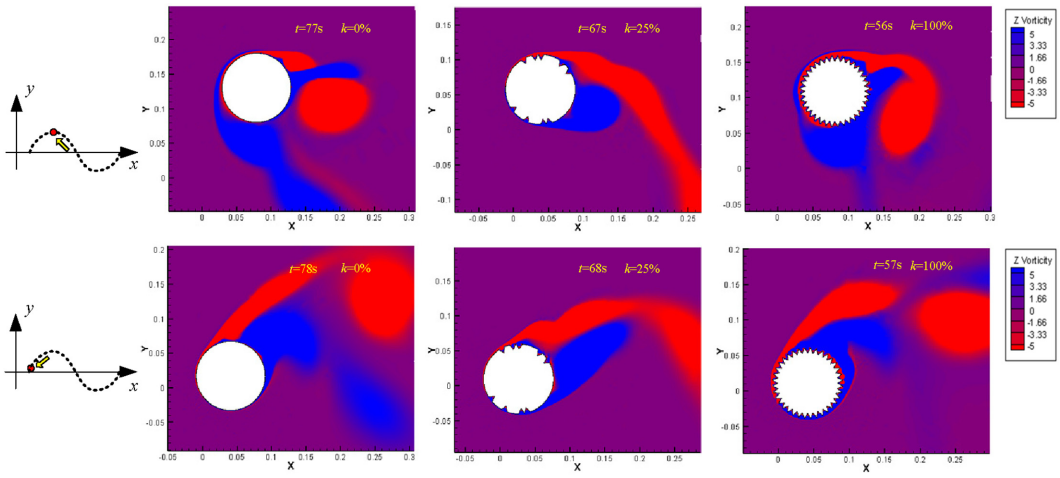

FIG. 25. Vorticity contours near the wall around the cylinder when approaching the highest point and the middle point (Coverage ratio $k = 0\%$, 25%, and 100%).

of the two vortices are opposite. For $k = 25\%$, the strength of the two reversed vortices is not equal due to the influence of random grooves, so the distribution of the main vortices is not symmetrical, which is also the reason why the vibration is suppressed. For $k = 100\%$, the vorticity contours are generally similar to $k = 0\%$, although a series of small vortices were generated in the random grooves.

The schematic diagrams of the vortex shedding structure around the cylinders with random grooves are presented in Fig. 26. Overall, the random and asymmetrical grooves reduce the strength of the main vortices. For $k = 25\%$ and $k = 50\%$, a small number of randomly distributed grooves result in smaller random vortices. These random vortices will not merge into a big vortex synchronously, so the driving force from the vortices is greatly reduced, and the VIV response becomes weaker. This phenomenon suggests that a small number of random grooves can significantly suppress the amplitude of the VIV response. For $k = 75\%$ and 100%, due to the larger number of random grooves, the grooves are almost filled with the cylinder. Each groove produces a small vortex, which generates backflow. When the backflow approaches the surface of the cylinder, the flow velocity decreases. Thus, the boundary layer looks thicker, and the thickness of vorticity near the surface also becomes thicker, as shown in Fig. 25 ($k = 0\%$ smooth cylinder and $k = 100\%$). For the VIV responses, the displacement of the mass-spring-damper system is a relative value, so the VIV responses are not very sensitive to the drag. The amplitude will only decrease slightly. These small vortices are distributed with similar laws and merge into large vortices, which is different from $k = 25\%$ and 50%. Specifically, although the strength of the large vortices is weakened, the vortices of $k = 100\%$ are similar to that of $k = 0\%$. Therefore, the amplitude of $k = 100\%$ is close to that of $k = 0\%$.

VI. CONCLUSIONS

Inspired by the rough tree bark, this study proposes a novel VIV suppression method with random grooves for the circular cylinder. The VIV response of the two-degree-of-freedom cylinder was solved based on a CFD solver and embedded codes. The simulation results have been compared with published data to verify the numerical method. The VIV responses of the cylinders with the groove coverage ratio $k = 0\%$, 25%, 50%, 75%, and 100% have been discussed in detail. The main conclusions are presented as follows:

(1) When the reduced velocity U^* increases from 2 to 15, the VIV response can be divided into the initial branch, upper branch, lower branch, and desynchronization region. The random grooves have a significant effect on vibration suppression, especially when $k = 25\%$. The maximum cross-flow amplitude ratio of $k = 25\%$ is only 0.65, which is reduced by 56.7% when compared with $k = 0\%$. The reattachment of the upstream vortices and the asymmetry of the vortices on both sides of the cylinder cause the unstable VIV response.
(2) The VIV response of the cylinder is not significantly suppressed when the coverage ratio k is 75%–100%. The VIV responses and flow structure of $k = 100\%$ and $k = 0\%$ have similar

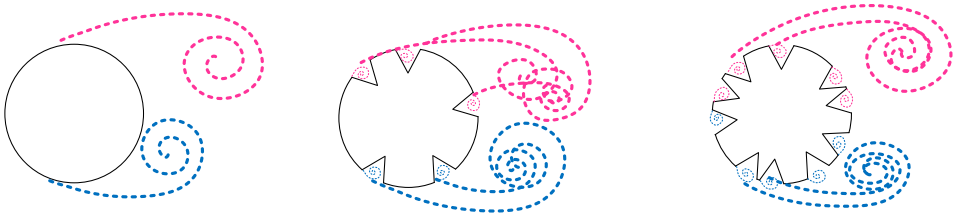

FIG. 26. Schematic diagrams of the vortex shedding structure around the cylinders with random grooves.

phenomena, but the amplitude of $k = 100\%$ is slightly smaller than k=0% due to the low strength of the shedding vortices.

(3) In general, when the vortex shedding frequency ratio is less than 1.0, the vortex pattern is the 2S mode. When the frequency ratio is higher than 1, the vortex pattern is the P+S/2P mode. Meanwhile, a jump phenomenon appears in the vortex phase, from 0° to 180°, which is closely related to the vortex pattern. In addition, the jump point increases with the groove coverage ratio.

(4) The VIV suppression mechanism of random grooves is revealed by analyzing the pressure distribution. A small number of random grooves resulted in asymmetrical and random vortices. These vortices will not merge into a large vortex and may cause unstable vibration. As a result, the driving force and the VIV response are suppressed, which can provide new methods for vibration suppression of slender cylinders and buildings.

Considering the complexity of the ocean environment and biodiversity, marine risers may not be suitable for this method. Because marine organisms attached to the surface of the column will gradually replenish the groove, the cost will be greatly increased by cleaning. In addition, the suppression effect is most pronounced when the coverage ratio is 25%. However, the location of random grooves is still relatively controversial and the variability of location with around 25% coverage ratio can be further discussed. In general, the random distribution of random grooves with inconsistent dimensions is also controversial. In addition, it is possible to apply a small number of random grooves and introduce again to go to other schemes to achieve a complement to in-line vibration suppression.

ACKNOWLEDGMENTS

This project was funded by the National Natural Science Foundation of China (Nos. 52201327, 52272360, and 52005288), China Postdoctoral Science Foundation (No. BX20200187), and National Science and Technology Major Project No. 2017-II-0004-0016.

AUTHOR DECLARATIONS

Conflict of Interest

The authors have no conflicts to disclose.

Author Contributions

Baoshou Zhang: Formal analysis (equal); Investigation (equal); Writing – original draft (equal). **Teng Long:** Methodology (equal). **Wei Wang:** Investigation (equal). **Renhe Shi:** Conceptualization (equal); Resources (equal). **Nianhui Ye:** Formal analysis (equal).

DATA AVAILABILITY

The data that support the findings of this study are available within the article.

REFERENCES

[1]T. Song, L. Ding, H. He, L. Zhang, and J. Ran, "Thermal fluid–structural interaction of three cylinders undergoing flow-induced vibration with cross thermal buoyancy," Phys. Fluids **34**(12), 123601 (2022).
[2]Z. P. Zang and F. P. Gao, "Steady current induced vibration of near-bed piggyback pipelines: Configuration effects on VIV suppression," Appl. Ocean Res. **46**, 62–69 (2014).
[3]A. K. Soti and A. De, "Vortex-induced vibrations of a confined circular cylinder for efficient flow power extraction," Phys. Fluids **32**(3), 033603 (2020).
[4]B. Seyed-Aghazadeh, H. Samandari, and S. Dulac, "Flow-induced vibration of inherently nonlinear structures with applications in energy harvesting," Phys. Fluids **32**(7), 071701 (2020).
[5]S. Rashidi, M. Bovand, I. Pop, and M. S. Valipour, "Numerical simulation of forced convective heat transfer past a square diamond-shaped porous cylinder," Transp. Porous Media **102**, 207–225 (2014).
[6]S. Rashidi, A. Nouri-Borujerdi, M. S. Valipour, R. Ellahi, and I. Pop, "Stress-jump and continuity interface conditions for a cylinder embedded in a porous medium," Transp. Porous Media **107**, 171–186 (2015).
[7]W. Zhong, S. C. Yim, and L. Deng, "Vortex shedding patterns past a rectangular cylinder near a free surface," Ocean Eng. **200**, 107049 (2020).
[8]C. Mannini, A. Šoda, and G. Schewe, "Unsteady RANS modelling of flow past a rectangular cylinder: Investigation of Reynolds number effects," Comput. Fluids **39**(9), 1609–1624 (2010).
[9]C. Norberg, "Flow around rectangular cylinders: Pressure forces and wake frequencies," J. Wind Eng. Ind. Aerodyn. **49**(1–3), 187–196 (1993).
[10]A. Okajima, "Strouhal numbers of rectangular cylinders," J. Fluid Mech. **123**, 379–398 (1982).
[11]G. Schewe, "Reynolds-number-effects in flow around a rectangular cylinder with aspect ratio 1: 5," J. Fluids Struct. **39**, 15–26 (2013).
[12]H. Wan and S. S. Patnaik, "Suppression of vortex-induced vibration of a circular cylinder using thermal effects," Phys. Fluids **28**(12), 123603 (2016).
[13]S. M. Hasheminejad and Y. Masoumi, "Smart hybrid VIV control of a linearly sprung cylinder using an internal semi-active NES-based vibration absorber coupled with two active rotating wake-control rods," Ocean Eng. **266**, 112310 (2022).
[14]A. Sohankar, M. Khodadadi, and E. Rangraz, "Control of fluid flow and heat transfer around a square cylinder by uniform suction and blowing at low Reynolds numbers," Comput. Fluids **109**, 155–167 (2015).
[15]A. H. Rabiee, "Two-degree-of-freedom flow-induced vibration suppression of a circular cylinder via externally forced rotational oscillations: Comparison of active open-loop and closed-loop control systems," J. Brazilian Soc. Mech. Sci. Eng. **42**, 470 (2020).
[16]T. L. Flinois and T. Colonius, "Optimal control of circular cylinder wakes using long control horizons," Phys. Fluids **27**(8), 087105 (2015).
[17]H. Zhu, T. Tang, H. Zhao, and Y. Gao, "Control of vortex-induced vibration of a circular cylinder using a pair of air jets at low Reynolds number," Phys. Fluids **31**(4), 043603 (2019).
[18]J. Chen and J. Wu, "Control of vortex-induced vibration of an elastically mounted cylinder with a pair of porous rods," Phys. Fluids **34**(12), 123610 (2022).
[19]Y. Gao, S. Fu, J. Wang, L. Song, and Y. Chen, "Experimental study of the effects of surface roughness on the vortex-induced vibration response of a flexible cylinder," Ocean Eng. **103**, 40–54 (2015).
[20]B. Zhou, X. Wang, W. M. Gho, and S. K. Tan, "Force and flow characteristics of a circular cylinder with uniform surface roughness at subcritical Reynolds numbers," Appl. Ocean Res. **49**, 20–26 (2015).
[21]J. Y. Shao, J. D. Wen, and L. Zhang, "Flow control of an elastically mounted square cylinder by using an attached flexible plate," Phys. Fluids **35**(3), 033603 (2023).
[22]W. Chen, C. Ji, D. Xu, and Z. Zhang, "Oscillation regimes and mechanisms in the vortex-induced vibrations of three circular cylinders with equilateral-triangular arrangements," Phys. Fluids **32**(4), 043602 (2020).
[23]H. Ren, Y. Xu, J. Cheng, P. Cao, M. Zhang, S. Fu, and Z. Zhu, "Vortex-induced vibration of flexible pipe fitted with helical strakes in oscillatory flow," Ocean Eng. **189**, 106274 (2019).
[24]H. Ping, H. Zhu, K. Zhang, D. Zhou, Y. Bao, and Z. Han, "Vortex-induced vibrations of two rigidly coupled circular cylinders of unequal diameters at low Reynolds number," Phys. Fluids **33**(10), 103603 (2021).
[25]T. Qiu, W. Lin, X. Du, and Y. Zhao, "Mass ratio effect on vortex-induced vibration for two tandem square cylinders at a low Reynolds number," Phys. Fluids **33**(12), 123604 (2021).
[26]G. R. Franzini, "An elastic rotative nonlinear vibration absorber (ERNVA) as a passive suppressor for vortex-induced vibrations," Nonlinear Dyn. **103**(1), 255–277 (2021).
[27]R. Wang, S. Cheng, and D. S. K. Ting, "Numerical study of roundness effect on flow around a circular cylinder," Phys. Fluids **32**(4), 044106 (2020).

[28]Y. Z. Law and R. K. Jaiman, "Passive control of vortex-induced vibration by spanwise grooves," J. Fluids Struct. **83**, 1–26 (2018).
[29]W. Wang, B. Song, Z. Mao, W. Tian, and T. Zhang, "Numerical investigation on VIV suppression of the cylinder with the bionic surface inspired by giant cactus," Ocean Eng. **214**, 107775 (2020).
[30]W. Wang, Z. Mao, B. Song, and W. Tian, "Suppression of vortex-induced vibration of a cactus-inspired cylinder near a free surface," Phys. Fluids **33**(6), 067103 (2021).
[31]W. Wang, Z. Mao, B. Song, and T. Zhang, "Vortex-induced vibration response of a cactus-inspired cylinder near a stationary wall," Phys. Fluids **33**(7), 077119 (2021).
[32]B. Zhang, B. Song, Z. Mao, W. Tian, and B. Li, "Numerical investigation on VIV energy harvesting of bluff bodies with different cross sections in tandem arrangement," Energy **133**, 723–736 (2017).
[33]B. Zhang, Z. Mao, B. Song, W. Ding, and W. Tian, "Numerical investigation on effect of damping-ratio and mass-ratio on energy harnessing of a square cylinder in FIM," Energy **144**, 218–231 (2018).
[34]N. M. Newmark, "A method of computation for structural dynamics," J. Eng. Mech. Div. **85**(3), 67–94 (1959).
[35]J. F. Deü and D. Matignon, "Simulation of fractionally damped mechanical systems by means of a Newmark-diffusive scheme," Comput. Math. Appl. **59**(5), 1745–1753 (2010).
[36]X. Deng, "Numerical simulation of vortex induced vibrations using PC Newmark-β-based fluid-structure interaction method," Doctoral dissertation (Zhejiang University, 2015).
[37]B. Zhang, B. Song, Z. Mao, B. Li, and M. Gu, "Hydrokinetic energy harnessing by spring-mounted oscillators in FIM with different cross sections: From triangle to circle," Energy **189**, 116249 (2019).
[38]B. Zhang, B. Li, S. Fu, Z. Mao, and W. Ding, "Vortex-Induced Vibration (VIV) hydrokinetic energy harvesting based on nonlinear damping," Renewable Energy **195**, 1050–1063 (2022).
[39]W. Wang, Z. Mao, B. Song, and P. Han, "Numerical investigation on vortex-induced vibration suppression of the cactus-inspired cylinder with some ribs," Phys. Fluids **33**(3), 037127 (2021).
[40]N. A. Jauvtis and C. H. K. Williamson, "The effect of two degrees of freedom on vortex-induced vibration at low mass and damping," J. Fluid Mech. **509**, 23–62 (2004).
[41]Z. Kang, C. Zhang, R. Chang, and G. Ma, "A numerical investigation of the effects of Reynolds number on vortex-induced vibration of the cylinders with different mass ratios and frequency ratios," Int. J. Naval Archit. Ocean Eng. **11**(2), 835–850 (2019).
[42]M. M. Bernitsas, "Harvesting energy by flow included motions," in *Springer Handbook of Ocean Engineering* (Springer, 2016), pp. 1163–1244.